Supplementary Information for

Large thermal reservoir in nascent intracluster gas at redshift 4.3

Correspondence: Dazhi Zhou (dzhou.astro@gmail.com)
This PDF contains: Supplementary Methods, Figures, Tables, and References.

Supplementary Methods

S1. ALMA data reduction

The ALMA and ACA Band-3 data were obtained under four different programs from the ALMA Science Archive (2015.1.01543.T; 2017.1.00273.S; 2022.1.00495.S; 2023.1.00124.S). The corresponding configurations, baseline ranges, frequency ranges, correlator modes, and on-source integration times are summarized in Supplementary Table 1.

For the observations carried out before 2020, we used the standard ALMA calibration script to re-calibrate the data with the latest ALMA pipeline (`CASA` version=6.6.1)[1,2]. We carefully compared difference between the old and new calibrated data in their phase uncertainties, root mean square (rms) errors, and dynamical ranges of the continuum images produced from individual Execution Blocks (EBs). In general, the calibrated data obtained from the new pipeline show a $\sim 5\%$ improvement in their dynamic range. Therefore, we adopted all measurement sets calibrated by the new pipeline for consistency.

We used the observatory-calibrated measurement sets for the Cycle 9 and Cycle 10 data, which were calibrated by `CASA` 6.4.1 and `CASA` 6.6.1, respectively. According to the QA2 report from the observatory, there was some potential cloud contamination in a fraction of EBs, leading to higher phase errors. We ran the `remcloud` [1] pipeline for better phase calibrations and inspected the improvement of the data quality. Only two EBs showed $\sim 20\%$ and $\sim 200\%$ improvements in their dynamical range after the `remcloud` correction, which were used in this study.

Each EB was assessed by comparing the flux densities of bright sources from the `CLEAN`ed image to ensure that the calibration was consistent. The calibration was good in general,with the amplitudes of bright sources differing by $< 5\%$ at the same frequency for all EBs except two EBs, where the higher phase errors of these data introduced a loss of coherence. The high phase errors caused reduced amplitudes and elevated rms noises due to decorrelation, instead of amplitude calibration errors. In fact, the affected EBs show good agreement with other EBs after tapering, indicating that higher phase errors are dominated by the long baselines, while short baselines still keep a good coherence. Despite their worse qualities, these two EBs are still included for better *uv*-coverage and large-scale sensitivity. We used 'natural' weighting for all `CLEAN`ing processes in the following analysis to suppress the long-baseline contribution.

Because the accumulated data size is over a few terabytes, some data compression was needed before imaging for a higher efficiency. The latest `CASA` (version=6.7.0) was used for both preprocessing and imaging. We used the `CASA` task `mstransform` to compress all data to a common frequency and time width of 62.5MHz and 8s, respectively. This approach greatly reduces the data size without causing the potential bandwidth- and time-smearing effect. The phase center of each measurement set was then shifted to the pointing center of the Cycle 10 program through `phase_shift` command. Subsequently, we combined all EBs obtained from the same cycle to a single measurement set using

[1] `https://help.almascience.org/kb/articles/what-is-remcloud-and-how-could-it-reduce-phase-rms`

the CASA task `concat` with `copypointing=False`. Channels with spectral lines were flagged by the task `flagdata`, which are listed in Supplementary Table 2.

Considering there are over 70 EBs with different tuning frequencies and configurations, caution is required to handle the visibility plane. The steep spectral slope of the dust continuum emission from the protocluster galaxies can lead to baseline-dependent flux densities, owing to the frequency variations of the different baselines, which can cause artificial signals in the Fourier-plane subtraction technique. We used all the data to produce ultra-deep continuum images for the direct tSZ decrement imaging ('Deep' and 'Deep (tapered)'), and used the subset of measurement sets with similar frequency ranges from Cycle 5 and Cycle 10 for source subtraction and tSZ measurements ('ALMA high-res', Supplementary Table 3).

The deep continuum map was generated with `tclean` using line-free channels, '`natural`' weighting, '`hogbom`' deconvolver, '`mosaic`' gridder in '`mfs`' mode. We applied a $2''$ uv taper to enhance sensitivity to extended emission. A two-step strategy was used for the `CLEAN`ing process. First, we `CLEAN`ed without a mask down to 4σ, ensuring real emission is deconvolved while avoiding noise spikes. Next, we masked the high-significance 4σ pixels and dilated them to the adjacent 2σ pixels. With this robust mask, we `CLEAN`ed the data to $\pm1\sigma$, which suppresses dirty-beam sidelobes and prevents over-`CLEAN`ing of noise spikes. The rms level of the `CLEAN`ed image is 1.8μJy/beam with a $2.4'' \times 2.1''$ synthesized beam before tapering, and 2.1μJy/beam with a $3.7'' \times 3.3''$ beam after tapering. In the 'Deep (tapered)' image (Supplementary Fig. 1), a negative halo around the protocluster galaxies reaches -4.5σ, which is also present in the `CLEAN`ed and the residual of the "Deep" image (Supplementary Fig. 2). The positive signal peaks at 116σ, which is comparable to the typical dynamic range achieved in ALMA Band-3 ($\sim 100\sigma$), supporting that features as faint as -4.5σ are reliable instead of an imaging artifact.

The tSZ signal is expected to contaminate the galaxies' continuum emission, which dominates the short spatial-frequency range. To produce a high-resolution continuum image for further source subtraction ('ALMA high-res'), we discarded the data with different frequency coverages (see Supplementary Table 3) and excluded all baselines with uv-distances less than $10\mathrm{k}\lambda$ to suppress the extended tSZ contamination while still maintaining a good sensitivity. Under such a uv-distance selection, all signals with spatial scales above $20''$ are greatly reduced. We selected the line-free channels and used the identical two-step `CLEAN`ing strategy to produce the continuum map (Supplementary Fig. 3). With this uv range-selection strategy, the continuum flux density of each source is increased by $0 \sim 15\,\mu$Jy (Supplementary Fig. 4), while the rms sensitivity only drops by $\sim 1\%$. The difference of the continuum level is also enhanced at the central region, supporting the existence of the extended tSZ decrement in SPT2349. The synthesized beam size of the continuum image is $2.2'' \times 1.9''$ and the rms sensitivity is 2.1μJy/beam.

For the direct comparison of dust continuum under different scales, we also produced two independent low-resolution images from the short baselines ($< 10k\lambda$) of ALMA ('ALMA low-res') and from the ACA observations in a similar manner. The sensitivities of 'ALMA low-res' and ACA continuum images are $11\,\mu$Jy/beam and $24\,\mu$Jy/beam. Their corresponding resolutions are $14.4'' \times 13.4''$ and $18.0'' \times 12.1''$, respectively.

The details of each image, including the on-source exposure time, is summarized in Supplementary Table 3. The Maximum Recoverable Scale (MRS) of each map was estimated from the corresponding spatial scale of the fifth percentile value of the ALMA baseline lengths[3,4]. The quoted value could overestimate the MRS when poorly-sample and less-weighted ACA data are included, which should be treated as the upper limit.

S2. Validation of the decrement with ALMA simulations

To test the reliability of the potential tSZ signatures, we conducted interferometric simulations using the `CASA` function `simalma`. We used the Band-7 catalog[5] as a prior and scaled the flux densities by $S_{3\mathrm{mm,total}}/S_{850\mu\mathrm{m,total}}$ to obtain the 3 mm flux density of each emissive source. As sensitivity can be underestimated by `simalma`, we tweaked the scaling factor of the telescope time in each configuration until the rms agreed with the actual value ($\Delta\mathrm{rms}/\mathrm{rms} < 5\%$). For a more realistic simulation, we also injected continuum sources on the jackknifed measurement sets, which were produced by inverting half of the visibilities to cancel the astrophysical signals.

Supplementary Fig. 5 shows the comparison between the simulations and the actual continuum image on the same scale. While the previous section reinforces the evidence of a tSZ decrement already seen as a negative halo in the real image, we also considered the possibility that the evidence of tSZ effect was caused by an interferometric artifact from combining different ALMA configurations. Although the issue of the negative sidelobes is greatly suppressed in such deep observations, imperfect `CLEAN`ing can be still expected, which may cause a similar negative halo. However, the coherent negative halo does not exist in the simulated image, where the minimum pixel value in the core region is only 4.5 μJy, 1.7σ less than the decrement peak (7.6 μJy) in the actual continuum image. Furthermore, we used the same uv-range ($uv < 10k\lambda$) to produce the low-resolution mock image and performed the photometry measurements in an identical way. The continuum flux density from the low-resolution simulated map is consistent with the integrated value from the high-resolution image, with the discrepancy $\lesssim 2\%$, contrary to the 20% drop seen in the real data. Therefore, a potential artifact is unlikely to result in the current evidence of the tSZ decrement.

S3. Redshift evolution of ICM in TNG-Cluster simulations

To further investigate if the strong tSZ signal in SPT2349−56 can be naturally reproduced by modern cosmological hydrodynamical simulations, we compared our measured tSZ signal with predictions from the TNG-Cluster [2] zoom-in simulations of massive galaxy clusters[6,7]. In brief, TNG-Cluster comprises a suite of 352 high-resolution re-simulations of massive clusters selected from a parent dark matter-only simulation with a box size of ~ 1 Gpc. The sample includes all clusters at $z = 0$ with $M_{200} > 10^{15}\,M_\odot$, along with a representative subset of lower-mass systems spanning $M_{200} \sim 10^{14.3}$–$10^{15.0}\,M_\odot$. As with the IllustrisTNG framework, TNG-Cluster employs the `AREPO` moving-mesh magnetohydrodynamics code[8,9], together with the TNG galaxy formation model[10,11], which self-consistently follows the evolution of gas, stars, supermassive black holes, chemical enrichment, and feedback from both stellar and AGN sources.

For this analysis, we used the TNG-Cluster predictions to compare the thermal component of the gas to that inferred for the SPT2349−56 protocluster core. Specifically, we computed the Compton-y parameter following the prescriptions in literature[7,12–15], which are virtually equivalent. For each gas cell, the y parameter (Υ_i) was computed as

$$\Upsilon_i = \frac{k_B \sigma_T}{m_e c^2} N_{e,i} T_i, \tag{1}$$

where k_B is Boltzmann's constant, σ_T the Thomson scattering cross-section, m_e the electron mass, and c the speed of light. Here, $N_{e,i}$ and T_i represent the number of electrons and the temperature of the i-th gas cell, respectively. The number of electrons was computed as $N_{e,i} = n_{e,i} m_i/\rho_i$, where $n_{e,i}$ is the electron number density, m_i is the gas cell mass, and ρ_i is the gas density.

[2] `www.tng-project.org/cluster`

In practice, we derived Υ_i for each gas cell using `InternalEnergy` (U), `ElectronAbundance` (X_e), and `Masses` (m_i) from the TNG-Cluster outputs. The temperature of each gas cell was then calculated as

$$T_i = \frac{U(1-\gamma)\mu}{k_B}, \tag{2}$$

where $\gamma = 5/3$ is the adiabatic index and μ is the mean molecular weight, given by:

$$\mu = \frac{4}{1 + 3X_H + 4X_H X_e} m_p, \tag{3}$$

with X_H the hydrogen mass fraction (assumed to be $X_H = 0.76$) and m_p the proton mass. The number of electrons was computed as:

$$N_{e,i} = \frac{n_{e,i} m_i}{\rho_i} = \frac{X_e X_H m_i}{m_p}. \tag{4}$$

To compute $N_{e,i}$ and T_i for each gas cell, we adopted a fixed hydrogen mass fraction of $X_H = 0.76$, following common assumptions in the literature[7,13]. Although one might expect a higher hydrogen fraction at earlier epochs, we verified that the median hydrogen abundance in gas cells associated with the TNG-Cluster halo at $z \sim 5$ remains close to $X_H \sim 0.76$.

The integrated tSZ signal for a given halo, expressed as $Y_{500} D_A^2$, was calculated by summing the Υ_i contributions (from Equation 1) of all gas cells within a spherical aperture of radius R_{500}. We then tracked the redshift evolution of this tSZ proxy by evaluating Y_{500} for the main progenitors of all 352 clusters identified at $z = 0$ within the TNG-Cluster suite. We traced Y_{500} of each cluster for every four snapshots and calculated the 16th, 50th, and 84th percentile values in each redshift bin. The evolution of the fraction of hot gas $> 10^7$ K within the R_{500} radius ($f_{\rm hot} = M_{\rm hot,500}/M_{500}$) was also recorded to investigate the simulation expectation for the hot gas at earlier epochs. The Y_{500} values were scaled by $M_{500}^{1.79}$ to removed the mass dependency[16].

We show the 16th-50th-84th percentile values of the mass-scaled Y_{500} and $f_{\rm hot}$ at $0 \leq z \leq 5$ for each redshift bin in Fig. 1 and Extended Data Fig. 9, respectively. As indicated by Fig. 1, the tSZ decrement observed in SPT2349−56 is also more than five times the value predicted by TNG-Cluster. Without assuming a very massive halo (Extended Data Fig. 9), the lower hot-gas fraction or a cooler ICM in TNG-Cluster is likely the reason of this discrepancy.

Supplementary Figures

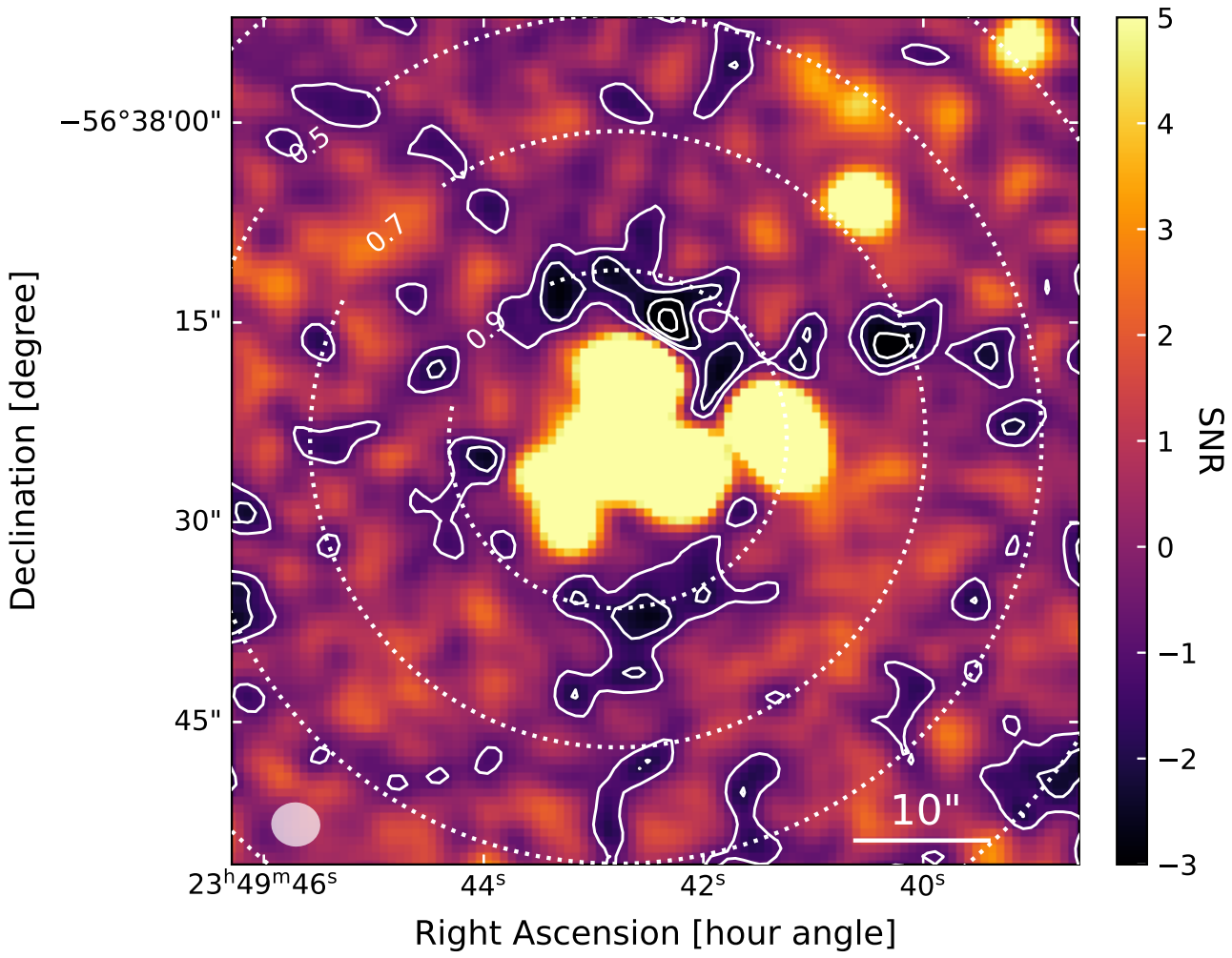

Supplementary Fig. 1: Tapered ALMA+ACA 3 mm continuum map. The positive signals come from dust emission of DSFGs. We use the contours from -1σ to -4σ with steps of -1σ to highlight the negative signals. The synthesized beam is shown in the bottom-left corner and the primary beam responses of 0.3, 0.5, 0.7, and 0.9 are indicated as dotted lines. A consistent negative ring is seen around the protocluster core, with a peak value at -4.5σ, suggesting the existence of extended tSZ signal.

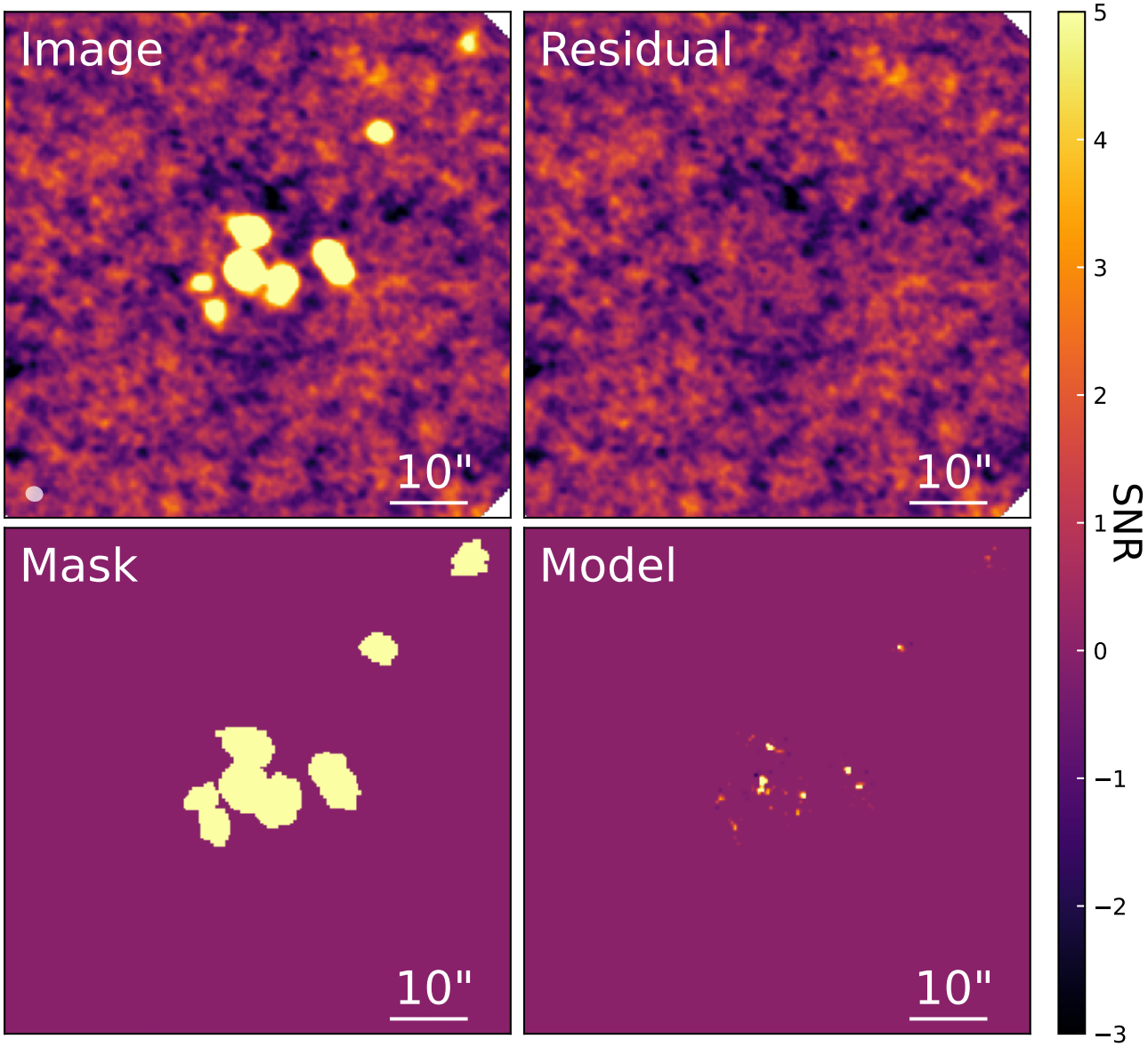

Supplementary Fig. 2: `CLEAN`ing process for the 'deep' imaging. To avoid negative sidelobes from the dirty beam, we performed a deep `CLEAN`ing down to the 1σ level, with the `CLEAN`ing mask and model indicated in the bottom panels. The synthesized beam is shown in the bottom-left corner of the upper-left panel. While the detected sources are well deconvolved, a diffuse negative halo remains visible in the residual map, demonstrating that this feature is not due to incomplete source subtraction.

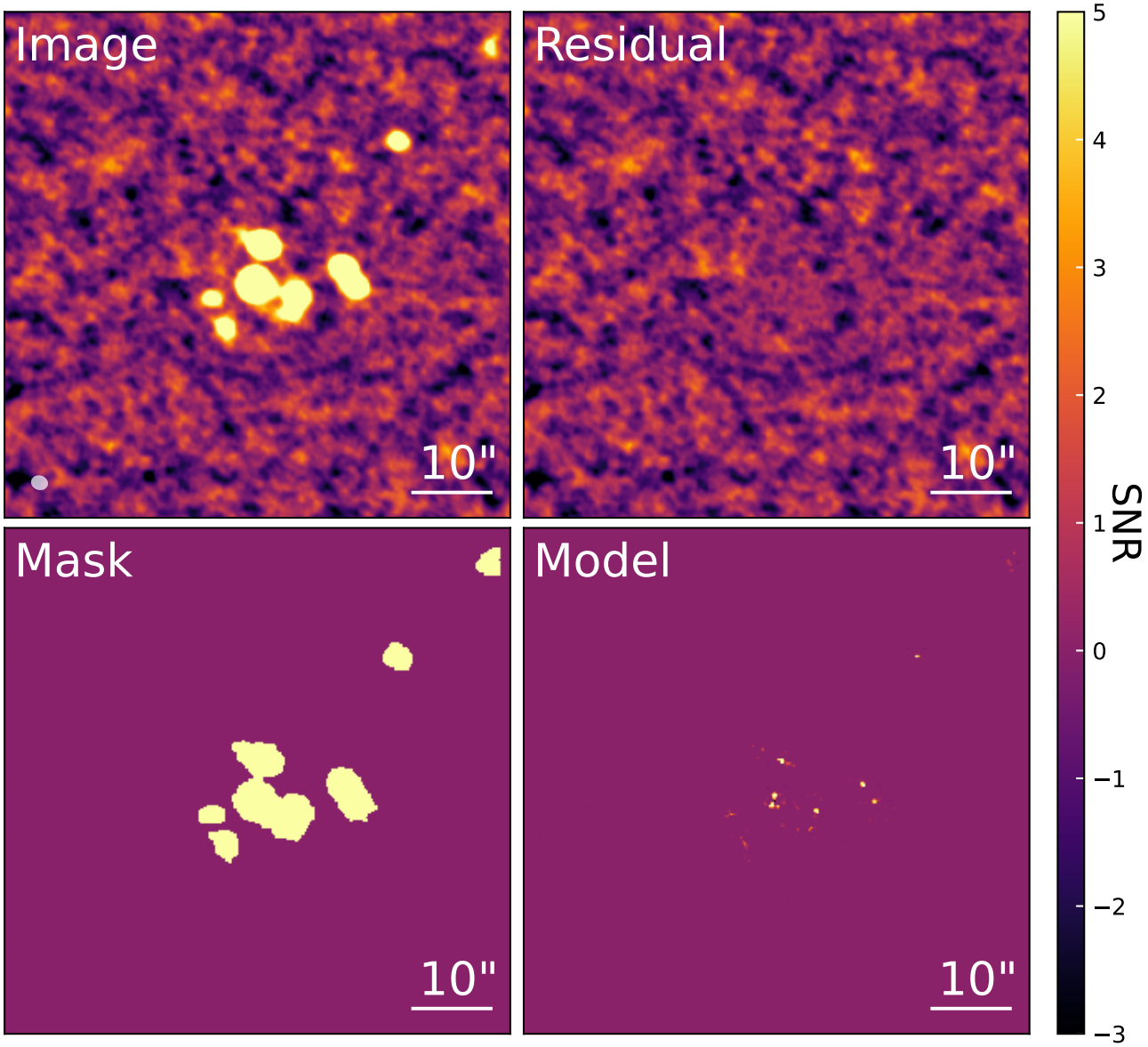

Supplementary Fig. 3: `CLEAN`ing process for the 'high-res' imaging. Same as Extended Data Fig. 2, but for the high-resolution imaging with short baselines excluded. The negative feature is not as prominent as in Extended Data Fig. 2, implying that the extended negative signal has been suppressed after excluding short baselines.

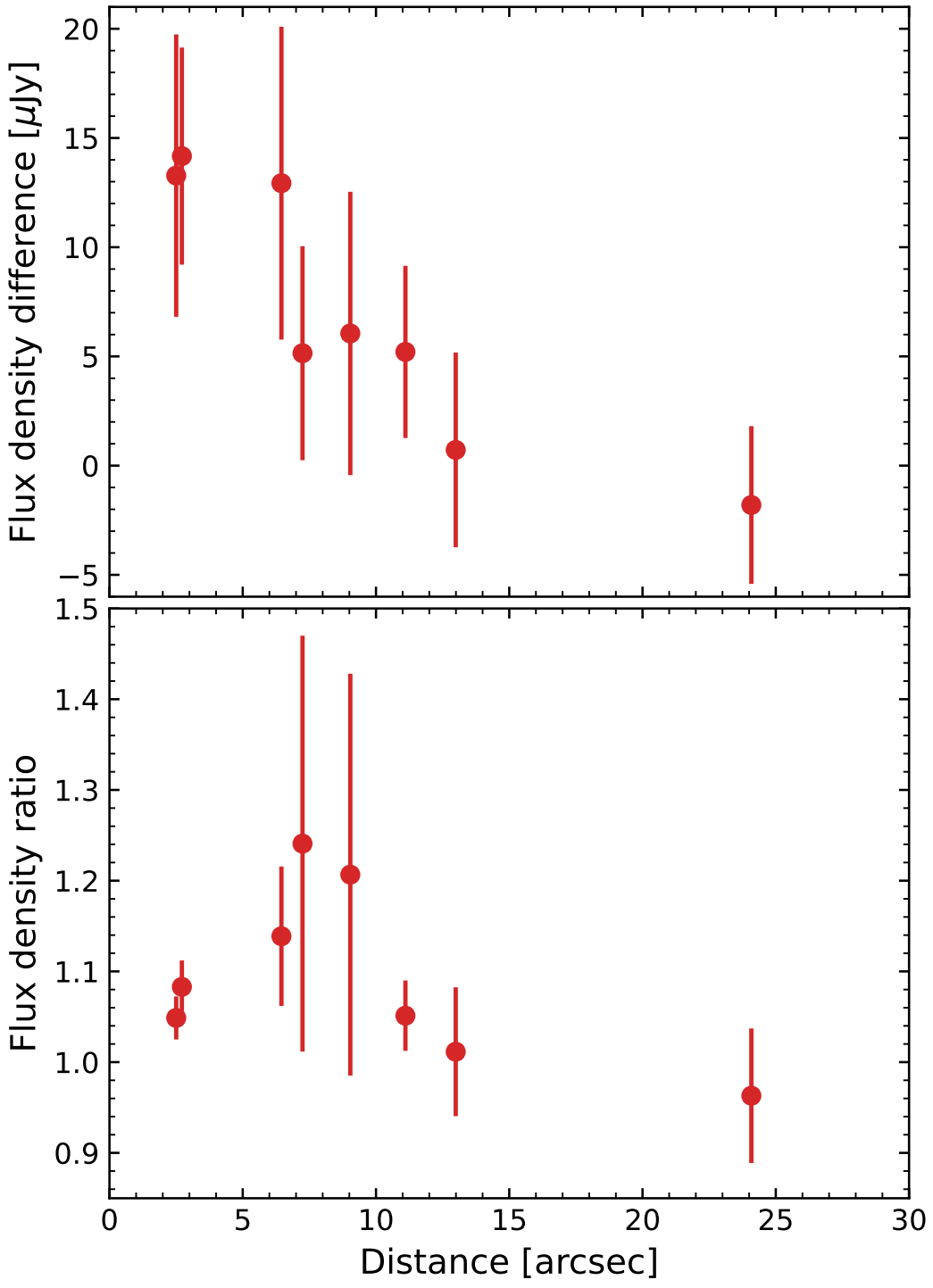

Supplementary Fig. 4: Effect of excluding short baselines on continuum flux densities. Flux density measurements of the galaxies before and after excluding short baselines ($< 10k\lambda$). The errorbars are derived from bootstrapping. *top:* Difference in continuum flux densities as a function of distance from the phase center. *bottom:* Corresponding flux density ratios of values after and before excluding short baselines. The systematic increase in continuum flux density toward the core region is consistent with the expected suppression of large-scale tSZ decrement when short baselines are removed.

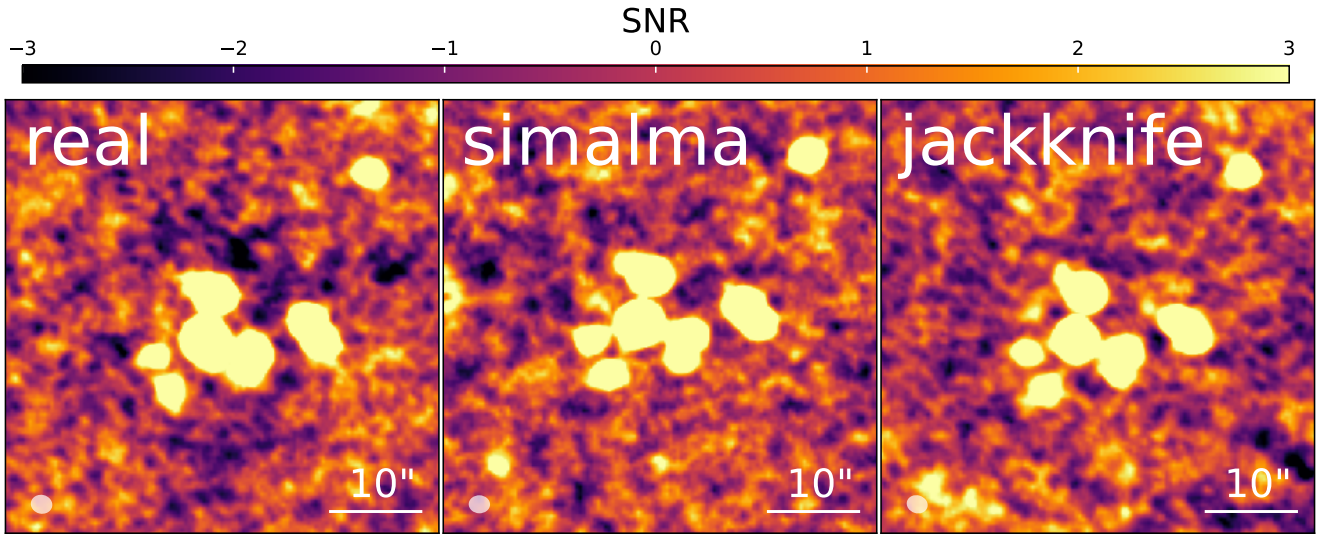

Supplementary Fig. 5: Comparison between the real and simulated images. We created simulated continuum images to further investigate if the negative halo can be caused by any unknown interferometric artifacts due to the complex distribution of the bright DSFGs. The corresponding synthesized beam is shown in the bottom-left corner for each panel. *left:* `CLEAN`ed image obtained from real visibilities. *middle:* `CLEAN`ed image obtained from simulated visibilities created by `simalma`. *right:* `CLEAN`ed image obtained by injecting model sources to signal-free jackknife visibilities, which were obtained through inverting half visibilities to cancel astronomical signals. The minimum pixel value from the real map is 1.7σ more significant than both simulated maps, and the simulated maps do not display a coherent negative ring seen in the real image.

Supplementary Tables

Supplementary Table 1: Summary of ALMA observations used in this study.

Program ID	Configuration	$L_{\rm base}$ [m]	Frequency coverage [GHz]	$t_{\rm source}$ [min]
2023.1.00124.S	12-m (C-3)	15–500	85.9–89.9, 97.9–101.9	685
2023.1.00124.S	12-m (C-4)	15–784	85.9–89.9, 97.9–101.9	49
2023.1.00124.S	12-m (C-2)	15–314	85.9–89.9, 97.9–101.9	49
2023.1.00124.S	7-m (ACA)	9–49	85.9–89.9, 97.9–101.9	1616
2022.1.00495.S	12-m (C-3)	15–368	89.1–92.9, 101.1–104.9	198
2022.1.00495.S	12-m (C-2)	15–313	89.1–92.9, 101.1–104.9	148
2017.1.00273.S	12-m (C43-4)	15–784	86.2–89.6, 97.9–101.6	47
2017.1.00273.S	12-m (C43-5)	15–1231	86.2–89.6, 97.9–101.6	116
2017.1.00273.S	12-m (C43-4)	15–784	89.8–93.7, 101.8–105.8	78
2015.1.01543.T	12-m (C40-4)	15–704	84.3–87.9, 96.4–100.0	47

Supplementary Table 2: Frequency range of the flagged channels in each tuning.

Program ID	Frequency coverage [GHz]	Flagged channels [GHz]	Flagged fraction
2023.1.00124.S	85.9–89.9, 97.9–101.9	86.5–87.35 (CO), 98.5–98.85 (foreground)	16%
2022.1.00495.S	89.1–92.9, 101.1–104.9	92.4–92.9 ([CI]), 103.1–104.3 (^{13}CO&C^{18}O)	23%
2017.1.00273.S	86.2–89.6, 97.9–101.6	86.5–87.35 (CO), 98.5–98.85 (foreground)	16%
2017.1.00273.S	89.8–93.7, 101.8–105.8	92.4–93.2 ([CI]), 103.1–104.3 (^{13}CO&C^{18}O)	27%
2015.1.01543.T	84.3–87.9, 96.4–100.0	86.5–87.35 (CO), 98.5–98.85 (foreground)	16%

Supplementary Table 3: Details of continuum maps used in this study.

Map	Used data	Frequency coverage [GHz]	uv-range [$k\lambda$]	Taper	$t_{\rm ALMA} + t_{\rm ACA}$ [min]	RMS [μJy/beam]	Beam [arcsec^2]	MRS [arcsec]
Deep	all	84.3–93.7, 96.4–105.8	2–400	N/A	1416+1616	1.8	2.4×2.1	33
Deep (tapered)	all	84.3–93.7, 96.4–105.8	2–400	2″	1416+1616	2.1	3.7×3.3	34
ALMA high-res	2023.1.00124.S	85.9–89.9, 97.9–101.9	10–220	N/A	782+0	2.1	2.2×1.9	16
	2017.1.00273.S	86.2–89.6, 97.9–101.6	10–400		163+0			
ALMA low-res	2023.1.00124.S	85.9–89.9, 97.9–101.9	4–10	N/A	782+0	11	14.4×13.4	48
	2017.1.00273.S	86.2–89.6, 97.9–101.6	4–10		163+0			
ACA	2023.1.00124.S	85.9–89.9, 97.9–101.9	2–14	N/A	0+1616	24	18.0×12.1	$\lesssim$76
SZ	2023.1.00124.S	84.3–87.9, 96.4–100.0	2–10	N/A	782+1616	8.8	13.6×14.7	$\lesssim$72
	2017.1.00273.S	86.2–89.6, 97.9–101.6	4–10		163+0			

References

[1] Hunter, T.R., Indebetouw, R., Brogan, C.L., Berry, K., Chang, C.-S., Francke, H., Geers, V.C., Gómez, L., Hibbard, J.E., Humphreys, E.M., Kent, B.R., Kepley, A.A., Kunneriath, D., Lipnicky, A., Loomis, R.A., Mason, B.S., Masters, J.S., Maud, L.T., Muders, D., Sabater, J., Sugimoto, K., Szűcs, L., Vasiliev, E., Videla, L., Villard, E., Williams, S.J., Xue, R., Yoon, I.: The ALMA Interferometric Pipeline Heuristics. **135**(1049), 074501 (2023) `https://doi.org/10.1088/1538-3873/ace216` arXiv:2306.07420 [astro-ph.IM]

[2] CASA Team, Bean, B., Bhatnagar, S., Castro, S., Donovan Meyer, J., Emonts, B., Garcia, E., Garwood, R., Golap, K., Gonzalez Villalba, J., Harris, P., Hayashi, Y., Hoskins, J., Hsieh, M., Jagannathan, P., Kawasaki, W., Keimpema, A., Kettenis, M., Lopez, J., Marvil, J., Masters, J., McNichols, A., Mehringer, D., Miel, R., Moellenbrock, G., Montesino, F., Nakazato, T., Ott, J., Petry, D., Pokorny, M., Raba, R., Rau, U., Schiebel, D., Schweighart, N., Sekhar, S., Shimada, K., Small, D., Steeb, J.-W., Sugimoto, K., Suoranta, V., Tsutsumi, T., van Bemmel, I.M., Verkouter, M., Wells, A., Xiong, W., Szomoru, A., Griffith, M., Glendenning, B., Kern, J.: CASA, the Common Astronomy Software Applications for Radio Astronomy. **134**(1041), 114501 (2022) `https://doi.org/10.1088/1538-3873/ac9642` arXiv:2210.02276 [astro-ph.IM]

[3] Remijan, A., Biggs, A., Cortes, P.A., Dent, B., Di Franceso, J., Fomalont, E., Hales, A., Kameno, S., Mason, B., Philips, N., Saini, K., Vila Vilaro, B., Villard, E.: ALMA Technical Handbook,ALMA Doc. 7.3, ver. 1.1. 2019, ALMA Technical Handbook,ALMA Doc. 7.3, ver. 1.1ISBN 978-3-923524-66-2 (2019). `https://doi.org/10.5281/zenodo.4511522`

[4] Czekala, I., Loomis, R.A., Teague, R., Booth, A.S., Huang, J., Cataldi, G., Ilee, J.D., Law, C.J., Walsh, C., Bosman, A.D., Guzmán, V.V., Le Gal, R., Öberg, K.I., Yamato, Y., Aikawa, Y., Andrews, S.M., Bae, J., Bergin, E.A., Bergner, J.B., Cleeves, L.I., Kurtovic, N.T., Ménard, F., Nomura, H., Pérez, L.M., Qi, C., Schwarz, K.R., Tsukagoshi, T., Waggoner, A.R., Wilner, D.J., Zhang, K.: Molecules with ALMA at Planet-forming Scales (MAPS). II. CLEAN Strategies for Synthesizing Images of Molecular Line Emission in Protoplanetary Disks. **257**(1), 2 (2021) `https://doi.org/10.3847/1538-4365/ac1430` arXiv:2109.06188 [astro-ph.EP]

[5] Hill, R., Chapman, S., Scott, D., Apostolovski, Y., Aravena, M., Béthermin, M., Bradford, C.M., Canning, R.E.A., De Breuck, C., Dong, C., Gonzalez, A., Greve, T.R., Hayward, C.C., Hezaveh, Y., Litke, K., Malkan, M., Marrone, D.P., Phadke, K., Reuter, C., Rotermund, K., Spilker, J., Vieira, J.D., Weiß, A.: Megaparsec-scale structure around the protocluster core SPT2349-56 at z = 4.3. **495**(3), 3124–3159 (2020) `https://doi.org/10.1093/mnras/staa1275` arXiv:2002.11600 [astro-ph.GA]

[6] Nelson, D., Springel, V., Pillepich, A., Rodriguez-Gomez, V., Torrey, P., Genel, S., Vogelsberger, M., Pakmor, R., Marinacci, F., Weinberger, R., Kelley, L., Lovell, M., Diemer, B., Hernquist, L.: The IllustrisTNG simulations: public data release. Computational Astrophysics and Cosmology **6**(1), 2 (2019) `https://doi.org/10.1186/s40668-019-0028-x` arXiv:1812.05609 [astro-ph.GA]

[7] Nelson, D., Pillepich, A., Ayromlou, M., Lee, W., Lehle, K., Rohr, E., Truong, N.: Introducing the TNG-Cluster simulation: Overview and the physical properties of the gaseous

intracluster medium. **686**, 157 (2024) https://doi.org/10.1051/0004-6361/202348608 arXiv:2311.06338 [astro-ph.GA]

[8] Springel, V.: E pur si muove: Galilean-invariant cosmological hydrodynamical simulations on a moving mesh. **401**(2), 791–851 (2010) https://doi.org/10.1111/j.1365-2966.2009.15715.x arXiv:0901.4107 [astro-ph.CO]

[9] Weinberger, R., Springel, V., Pakmor, R.: The AREPO Public Code Release. **248**(2), 32 (2020) https://doi.org/10.3847/1538-4365/ab908c arXiv:1909.04667 [astro-ph.IM]

[10] Weinberger, R., Springel, V., Hernquist, L., Pillepich, A., Marinacci, F., Pakmor, R., Nelson, D., Genel, S., Vogelsberger, M., Naiman, J., Torrey, P.: Simulating galaxy formation with black hole driven thermal and kinetic feedback. **465**(3), 3291–3308 (2017) https://doi.org/10.1093/mnras/stw2944 arXiv:1607.03486 [astro-ph.GA]

[11] Pillepich, A., Springel, V., Nelson, D., Genel, S., Naiman, J., Pakmor, R., Hernquist, L., Torrey, P., Vogelsberger, M., Weinberger, R., Marinacci, F.: Simulating galaxy formation with the IllustrisTNG model. **473**(3), 4077–4106 (2018) https://doi.org/10.1093/mnras/stx2656 arXiv:1703.02970 [astro-ph.GA]

[12] Roncarelli, M., Moscardini, L., Borgani, S., Dolag, K.: The Sunyaev-Zel'dovich effects from a cosmological hydrodynamical simulation: large-scale properties and correlation with the soft X-ray signal. **378**(4), 1259–1269 (2007) https://doi.org/10.1111/j.1365-2966.2007.11914.x arXiv:astro-ph/0701680 [astro-ph]

[13] Kay, S.T., Peel, M.W., Short, C.J., Thomas, P.A., Young, O.E., Battye, R.A., Liddle, A.R., Pearce, F.R.: Sunyaev-Zel'dovich clusters in Millennium gas simulations. **422**(3), 1999–2023 (2012) https://doi.org/10.1111/j.1365-2966.2012.20623.x arXiv:1112.3769 [astro-ph.CO]

[14] McCarthy, I.G., Le Brun, A.M.C., Schaye, J., Holder, G.P.: The thermal Sunyaev-Zel'dovich effect power spectrum in light of Planck. **440**(4), 3645–3657 (2014) https://doi.org/10.1093/mnras/stu543 arXiv:1312.5341 [astro-ph.CO]

[15] Bigwood, L., Bourne, M.A., Irsic, V., Amon, A., Sijacki, D.: The case for large-scale AGN feedback in galaxy formation simulations: insights from XFABLE. arXiv e-prints, 2501–16983 (2025) https://doi.org/10.48550/arXiv.2501.16983 arXiv:2501.16983 [astro-ph.CO]

[16] Planck Collaboration, Ade, P.A.R., Aghanim, N., Armitage-Caplan, C., Arnaud, M., Ashdown, M., Atrio-Barandela, F., Aumont, J., Baccigalupi, C., Banday, A.J., Barreiro, R.B., Barrena, R., Bartlett, J.G., Battaner, E., Battye, R., Benabed, K., Benoît, A., Benoit-Lévy, A., Bernard, J.-P., Bersanelli, M., Bielewicz, P., Bikmaev, I., Blanchard, A., Bobin, J., Bock, J.J., Böhringer, H., Bonaldi, A., Bond, J.R., Borrill, J., Bouchet, F.R., Bourdin, H., Bridges, M., Brown, M.L., Bucher, M., Burenin, R., Burigana, C., Butler, R.C., Cardoso, J.-F., Carvalho, P., Catalano, A., Challinor, A., Chamballu, A., Chary, R.-R., Chiang, L.-Y., Chiang, H.C., Chon, G., Christensen, P.R., Church, S., Clements, D.L., Colombi, S., Colombo, L.P.L., Couchot, F., Coulais, A., Crill, B.P., Curto, A., Cuttaia, F., Da Silva, A., Dahle, H., Danese, L., Davies, R.D., Davis, R.J., de Bernardis, P., de Rosa, A., de Zotti, G., Delabrouille, J., Delouis, J.-M., Démoclès, J., Désert, F.-X., Dickinson, C., Diego, J.M., Dolag, K., Dole, H., Donzelli, S., Doré, O., Douspis, M., Dupac, X., Efstathiou, G., Enßlin, T.A., Eriksen, H.K., Finelli, F.,

Flores-Cacho, I., Forni, O., Frailis, M., Franceschi, E., Fromenteau, S., Galeotta, S., Ganga, K., Génova-Santos, R.T., Giard, M., Giardino, G., Giraud-Héraud, Y., González-Nuevo, J., Górski, K.M., Gratton, S., Gregorio, A., Gruppuso, A., Hansen, F.K., Hanson, D., Harrison, D., Henrot-Versillé, S., Hernández-Monteagudo, C., Herranz, D., Hildebrandt, S.R., Hivon, E., Hobson, M., Holmes, W.A., Hornstrup, A., Hovest, W., Huffenberger, K.M., Hurier, G., Jaffe, T.R., Jaffe, A.H., Jones, W.C., Juvela, M., Keihänen, E., Keskitalo, R., Khamitov, I., Kisner, T.S., Kneissl, R., Knoche, J., Knox, L., Kunz, M., Kurki-Suonio, H., Lagache, G., Lähteenmäki, A., Lamarre, J.-M., Lasenby, A., Laureijs, R.J., Lawrence, C.R., Leahy, J.P., Leonardi, R., León-Tavares, J., Lesgourgues, J., Liddle, A., Liguori, M., Lilje, P.B., Linden-Vørnle, M., López-Caniego, M., Lubin, P.M., Macías-Pérez, J.F., Maffei, B., Maino, D., Mandolesi, N., Marcos-Caballero, A., Maris, M., Marshall, D.J., Martin, P.G., Martínez-González, E., Masi, S., Matarrese, S., Matthai, F., Mazzotta, P., Meinhold, P.R., Melchiorri, A., Melin, J.-B., Mendes, L., Mennella, A., Migliaccio, M., Mitra, S., Miville-Deschênes, M.-A., Moneti, A., Montier, L., Morgante, G., Mortlock, D., Moss, A., Munshi, D., Naselsky, P., Nati, F., Natoli, P., Netterfield, C.B., Nørgaard-Nielsen, H.U., Noviello, F., Novikov, D., Novikov, I., Osborne, S., Oxborrow, C.A., Paci, F., Pagano, L., Pajot, F., Paoletti, D., Partridge, B., Pasian, F., Patanchon, G., Perdereau, O., Perotto, L., Perrotta, F., Piacentini, F., Piat, M., Pierpaoli, E., Pietrobon, D., Plaszczynski, S., Pointecouteau, E., Polenta, G., Ponthieu, N., Popa, L., Poutanen, T., Pratt, G.W., Prézeau, G., Prunet, S., Puget, J.-L.: Planck 2013 results. XX. Cosmology from Sunyaev-Zeldovich cluster counts. **571**, 20 (2014) https://doi.org/10.1051/0004-6361/201321521 arXiv:1303.5080 [astro-ph.CO]